Design Principles of Permanent Magnet Synchronous Machines for Parallel Hybrid or Traction Applications

Katteden Kamiev, Juho Montonen, Mahendarkar Prabhakaran Ragavendra, Juha Pyrhönen, *Member, IEEE*, Juan A. Tapia, *Member, IEEE*, and Markku Niemelä

Abstract—Hybrid and full electric technologies are fast emerging in vehicles and mobile working machines, where electric machines and internal combustion engines are used together to power the systems. Permanent magnet (PM) technology plays an important role here despite the high magnet prices. This paper theoretically and empirically studies the design principles of PM synchronous machines (PMSMs) for hybrid applications, where a high starting torque and a wide field weakening range are needed. Several embedded-magnet PMSM magnetic circuit topologies are considered as possible candidates. A 10-kW PMSM prototype was built and tested. Experimental results verify the theoretical considerations well.

Index Terms—Inductance difference, parallel hybrid application, permanent magnet synchronous machine (PMSM), traction application.

I. INTRODUCTION

HIGH ENERGY efficiency and low emissions are the driving forces in electric vehicles and hybrid mobile work machines. It is possible to significantly improve the energy efficiency of a working machine or a vehicle by replacing a pure internal combustion engine (ICE) drive with a hybrid drive equipped with an ICE capable of producing the average power needed by the system. For example, a traditional passenger car moves at a 100-km/h speed with about 15-kW power on a smooth asphalted road built on a flat terrain and, from the energy efficiency point of view, car ICEs are largely overdimensioned just to achieve high acceleration, climbing ability, and maximum speed. The best benefit of the hybrid technologies is that they allow downsizing the ICE, resulting in significantly lower fuel consumption [1].

A design based on a driving cycle is studied, e.g., in [2]. A work machine may, e.g., be equipped with 165-kW diesel while
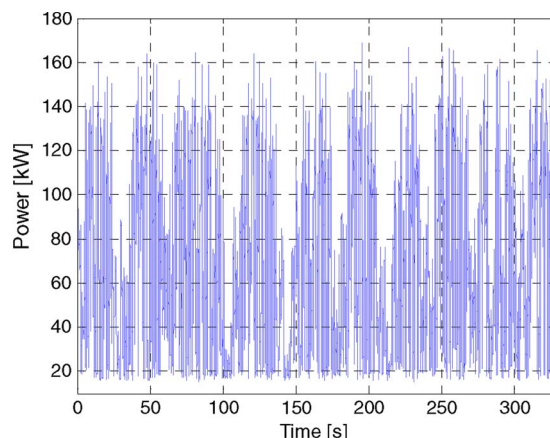

Fig. 1. Example of a work machine diesel operating cycle with 165-kW peak power and approximately 60-kW average power [3]. This cycle is a real cycle of a heavy-duty machine, not a simulated one.
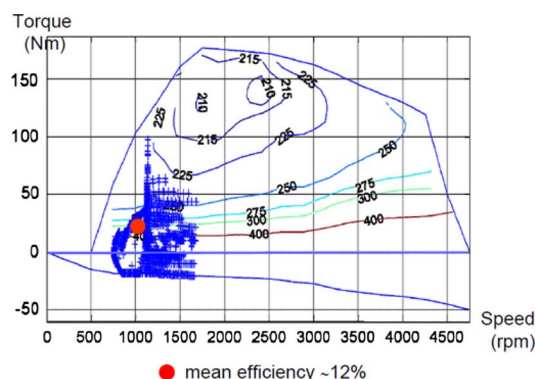

Fig. 2. Operation of a car diesel: an urban drive cycle iso-consumption (unit in gram/kilowatthour) map [4].

the average power consumption of the drive is far below 60 kW (see Fig. 1).

Fig. 2 shows an example of the efficiency map of a vehicle ICE and its operating points for an urban drive cycle. The actual operating cycle mean efficiency is only 12%. In an extra-urban drive cycle, the mean efficiency is somewhat better, which is about 20% [4]. In the best point, 210 g/kWh of 42- to 44-MJ/kg fuel is consumed, corresponding to ca. 40% efficiency. Hybridization with an appropriate energy storage makes ICE downsizing possible if continuous high-power performance is not required [5]. In addition, regenerative braking

K. Kamiev, J. Montonen, J. Pyrhönen, and M. Niemelä are with the Department of Electrical Engineering, Lappeenranta University of Technology, 53851 Lappeenranta, Finland (e-mail: katteden.kamiev@lut.fi; juho.montonen@lut.fi; juha.pyrhonen@lut.fi; markku.niemela@lut.fi).

M. P. Ragavendra is with M/s Lucas-TVS Ltd., Chennai-600004, India (e-mail: mpr.engg@lucastvs.co.in).

J. A. Tapia is with the University of Concepcion, Concepcion, Chile, and also with Lappeenranta University of Technology, 53851 Lappeenranta, Finland (e-mail: juan.tapia@lut.fi).

(or equivalent) makes an important contribution to energy saving in hybrid systems.

There are several different definitions for hybrid systems starting from micro and mild hybrids and ending up in full or heavy hybrid applications [6], [7]. These definitions are vague, and only parallel and series hybrids or their combinations are clear by definition. In parallel hybrids, as the operational speed range of the ICE is normally wide (e.g., idling at 750 min^{-1} and maximum speed of 4500 min^{-1}, see Fig. 2) and the torque production capability in the lower speed range is poor, the rated point of the electric machine (EM) is normally selected at a low speed, e.g., at one third of the ICE's maximum speed.

The simplest way to hybridize a vehicle is to keep the original mechanical power transmission, reduce the ICE, and attach an EM to the ICE crankshaft. In such a parallel hybrid case, only one EM is needed. The EM works both as a motor and a generator, depending on the operating cycle phase. In a normal passenger car, the cranking speed is about $100-150$ min^{-1}($n \approx$ 0.1 p.u.). The rated power of the EM must be achieved, for instance, at 1500 min^{-1}($n = 1$ p.u.); and the maximum operating speed of the machine should be, for example, 4500 min^{-1}($n = 3$ p.u.).

Similar requirements also hold for a traction motor [8]–[17]. Different permanent magnet (PM) excited rotor topologies for traction motors are presented and compared, for instance, in [18] and [19]. We study and discuss different embedded-magnet machine topologies for hybrid applications. The final selection is based on the best overall performance of the machine. To evaluate different machine designs, finite-element analyses (FMAs) are performed using the Flux 2D software package by Cedrat, Ltd. A 10-kW PM synchronous machine (PMSM) prototype, following the guidelines, is built and tested. Experimental results are reported and discussed.

II. BOUNDARY CONDITIONS

Here, the boundary conditions set by a parallel hybrid drive or a traction machine are considered.

A. Torque/Power-Speed Characteristic

Fig. 3 shows typical power and torque requirements of a traction machine in per unit values. At speeds lower than the rated speed, the torque and power are for intermittent use because of thermal limitations. At speeds higher or equivalent to the rated speed, the power is the maximum constant power. Depending on the inverter size, the peak torque can be two or even three times the EM rated torque. The rated torque and speed result in a rated heat rise in the machine. In Fig. 3, the peak torque is three times the rated torque. With constant power, the torque at the maximum speed is $1/n_{\mathrm{max,pu}}$ times the rated torque. The selection of the maximum speed has no exact mathematical explanation, but it is based on the practical optimization of the total costs and the performance of the system. An optimum speed ratio, that is, the ratio of the maximum to the rated speed of PMSMs applied to hybrid electric vehicle propulsion by taking into account the motor performance, viz., the peak
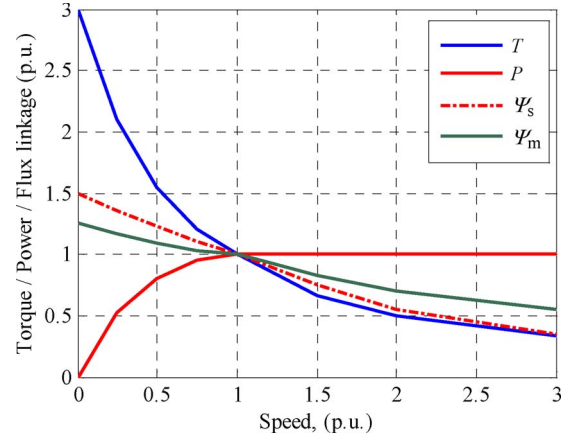

Fig. 3. Power P and torque T requirements of the machine in per unit and possible behavior of the stator flux linkage ψ_s and the air gap flux linkage ψ_m during maximum performance operation.

power, continuous power, total mass (volume), losses, and average efficiency were studied, for instance, in [20]. According to it, the PMSM optimum speed ratio falls within the range from 3.0 to 4.0 p.u. Therefore, based on this conclusion, the maximum speed is selected three times the rated speed. In a parallel hybrid application, as the EM is on the crankshaft of the ICE and it rotates at the same speed, the maximum speed of the ICE is taken as a boundary condition for the EM.

In low-speed operation, the maximum torque output is achieved by using a large stator current i_s and possibly by simultaneously increasing the air gap flux linkage ψ_m to increase the proportion of the reluctance torque, depending on the machine magnetizing inductances. The stator flux linkage ψ_s will automatically increase as a result of the armature reaction during high torque operation at low speeds. The back electromotive force (EMF) $e_s = \psi_s \omega_s$ is small at the lowest angular velocities ω_s; and therefore, despite an increased flux linkage, there is plenty of voltage reserve, i.e.,

$$u_{\mathrm{res}} = u_{\mathrm{max}} - \psi_s \omega_s \qquad (1)$$

in the low-speed operation range. After having reached the rated speed $\omega_s = \omega_{\mathrm{rated}}$, the stator voltage u_s is limited to some fixed values below 1 p.u. to maintain a suitable voltage reserve u_{res}, and the field weakening has to start. ψ_s must be reduced to about one third, when the speed is 3 p.u., to meet the voltage limitation u_{max}. This is achieved by using a negative d-axis current i_d and, simultaneously, by keeping the quadrature-axis armature reaction limited. At the same time, the resulting air gap flux linkage will decrease depending on the d- and q-axes magnetizing inductances L_{md} and L_{mq}, respectively, and the stator leakage inductance $L_{s\sigma}$ values.

In a rotor surface magnet machine, there is no reason to increase the air gap flux linkage deliberately because the torque of a rotor surface magnet machine is produced only by the quadrature-axis current i_q and the PM flux linkage ψ_{PM}. Thus

$$\boldsymbol{T}_e = \frac{3}{2}p\boldsymbol{\psi}_s \times \boldsymbol{i}_s \Rightarrow T_e = \frac{3}{2}p\psi_{\mathrm{PM}}i_q. \qquad (2)$$

Therefore, only the flux linkage generated by the PMs and the q-axis current produces a torque. However, a reluctance-torque-assisted PM machine (RTPM) can significantly benefit from the increase in the stator flux linkage at low speeds because the torque of such a machine is written as

$$\boldsymbol{T}_e = \frac{3}{2}p\boldsymbol{\psi}_s \times \boldsymbol{i}_s = \frac{3}{2}p\left(\psi_{\mathrm{PM}}i_q + (L_d - L_q)i_d i_q\right). \quad (3)$$

If we try to maximize the reluctance torque, we can call the machine an RTPM machine, where the PM torque, however, remains as the main torque [21]. As the i_d component in the RTPMs during motoring is negative, there will be an extra positive torque created by the latter components in (3). It is beneficial to increase the air gap flux linkage of an RTPM machine when the highest torques must be produced.

From (3), it is evident that, by making $(L_d - L_q)$ large negative (with L_d as small as possible, which is based on the synchronous machine load angle equation), a large motor reluctance torque is achieved. For this reason, when designing the RTPM, it is important to find a magnetic circuit design that makes the $(L_d - L_q)$ large enough by an absolute value.

B. Other Boundary Conditions

Hybrid and traction machines must usually have as low active material volume and mass as possible. Such a desire will lead to a large PM pole number because, as a result, small yokes and short end windings will be obtained. An eight-pole configuration with the number of slots per pole and phase $q = 2$ can be used as a starting point for a 10-kW machine. With increased pole numbers, both L_d and L_q will be reduced, and therefore, the inductance difference approaches zero as the pole pair number increases [22]. A compromise between the dimensions and the reluctance torque performance has to be made.

III. SUITABLE MACHINE PARAMETERS AND CORRESPONDING MACHINE TOPOLOGIES

The field weakening range limitation sets a clear boundary condition. At no-load operation, in principle, an infinite speed [23] can be found if the negative d-axis current can totally remove the stator flux linkage as

$$\psi_{\mathrm{PM}} - L_{sd,\min}i_{sd,\max} = 0. \quad (4)$$

From (4), we get a rule that, as continuous $i_{sd,\max} = 1$, in per unit

$$|\psi_{\mathrm{PM}}| = |L_{sd,\min}|. \quad (5)$$

If the maximum speed is 3 p.u. and the voltage reserve is chosen to be, e.g., 5%, the stator flux linkage maximum at this speed must be selected as

$$\psi_{s,\max} = \frac{u_{s,\max}}{\omega_{s,\max}} = \frac{0.95}{3} = 0.317 \text{ p.u.} \quad (6)$$

To achieve such a flux linkage level in no-load operation, we can find the minimum value for the direct-axis synchronous

TABLE I
MACHINE DESIGN REQUIREMENTS

Parameter	Value	Unit
Phase value, m	3	-
Rated power, P_{n}	10	kW
Rated phase voltage, U_{ph}	49	V
Rated frequency, f	100	Hz
Rated rotational speed, n_{n}	1500	min^{-1}
Outer stator diameter, D_{se}	252	mm
Machine stack length, l	40	mm

Design A
$L_{\mathrm{d}} - L_{\mathrm{q}} = -0.21$

Design B
$L_{\mathrm{d}} - L_{\mathrm{q}} = -0.32$

Design C
$L_{\mathrm{d}} - L_{\mathrm{q}} = -0.55$

Design D
$L_{\mathrm{d}} - L_{\mathrm{q}} = -0.51$

Design E
$L_{\mathrm{d}} - L_{\mathrm{q}} = -0.41$
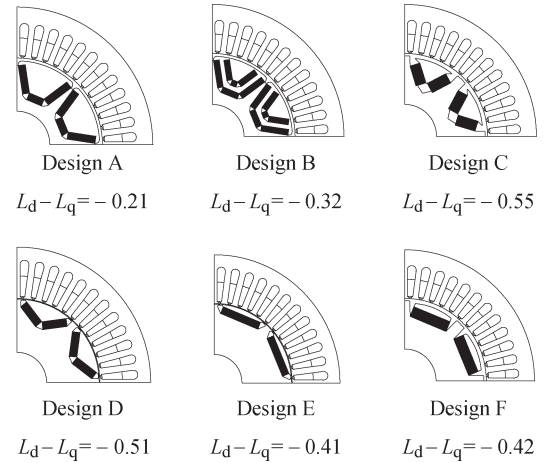
Design F
$L_{\mathrm{d}} - L_{\mathrm{q}} = -0.42$

Fig. 4. Studied topologies with embedded magnets.

inductance and the maximum value of the PM flux linkage. Let us preliminarily select $\psi_{\mathrm{PM}} = 0.8$ p.u. Thus

$$L_{d,\min} = \frac{\psi_{\mathrm{PM}} - \psi_{s,\max}}{i_{sd,\max}} = \frac{0.8 - 0.317}{1} = 0.483 \text{ p.u.} \quad (7)$$

In the following, examples of the studied topologies with embedded magnets are presented. Embedded design geometries resembling synchronous reluctance machines by a rotor design have been selected. Table I gives initial conditions. The rated phase voltage U_{ph} in a star-coupled three-phase system is 49 V (RMS) with a 120-V dc battery. The size of the outer diameter D_{se} and the machine stack length l were provided by the company providing the prototype.

The design results of the proposed machine topologies are reported in Fig. 4. The main idea has been to create flux barrier solutions that should produce small d-axis and high q-axis inductances for the PMSM. Designs C and D have the largest inductance differences. Designs C and F are theoretically good but are difficult to manufacture. From the economical point of view, Design B, in comparison with Designs A, D, and E, seems inefficient because of the second layer of PMs.

The PM flux linkage and the values for the inductances for different designs are given in Table II.

Usually, it is assumed that, below the rated speed ($n = 1$ p.u.), U_s/f is constant and, over it, the voltage is equal to $u_s = 1$ p.u.. The stator current, for the whole speed range, is

TABLE II
MACHINE PARAMETERS

Design A	Design B	Design C
$\psi_{PM} = 0.85$ p.u.	$\psi_{PM} = 0.80$ p.u.	$\psi_{PM} = 0.78$ p.u.
$L_d = 0.37$ p.u.	$L_d = 0.38$ p.u.	$L_d = 0.45$ p.u.
$L_q = 0.58$ p.u.	$L_q = 0.7$ p.u.	$L_q = 1.0$ p.u.

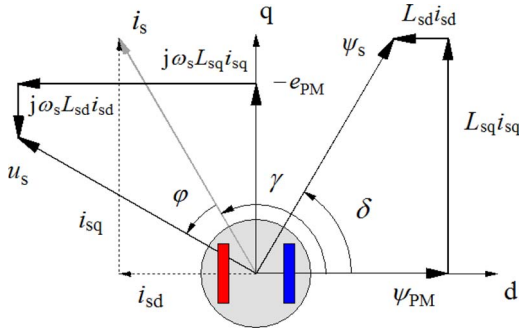| Design D	Design E	Design F
$\psi_{PM} = 0.77$ p.u.	$\psi_{PM} = 0.75$ p.u.	$\psi_{PM} = 0.76$ p.u.
$L_d = 0.49$ p.u.	$L_d = 0.45$ p.u.	$L_d = 0.40$ p.u.
$L_q = 1.0$ p.u.	$L_q = 0.86$ p.u.	$L_q = 0.82$ p.u.

Fig. 5. Vector diagram of a salient-pole synchronous motor with embedded magnets. The stator resistance is neglected.

settled to its rated value ($i_s = 1$ p.u.) to achieve a suitable operating temperature for the machine. Short overloading periods are allowed during low-speed operation.

To find the power capability curve, let us consider the vector diagram of a lossless inversely salient-pole synchronous motor, as shown in Fig. 5. u_s is the vector of the supplied terminal voltage; e_{PM} is the induced voltage; L_{sd} and L_{sq} are d- and q-axes synchronous inductances, respectively; i_s is the vector of the stator current; γ is the current angle measured from the d-axis; φ is the power factor angle; and δ is the load angle.

To follow the maximum torque per amperes, the current angle γ should be controlled so that the maximum output torque per ampere is obtained. It is found by setting

$$T|_{max} \rightarrow \frac{\partial T}{\partial \gamma} = 0,$$

$$\frac{\partial T}{\partial \gamma} = i_s e_{PMN} \cos \gamma_{opt1} + \omega_s (L_{sq} - L_{sd}) i_s^2 \cos 2\gamma_{opt1} = 0. \tag{8}$$
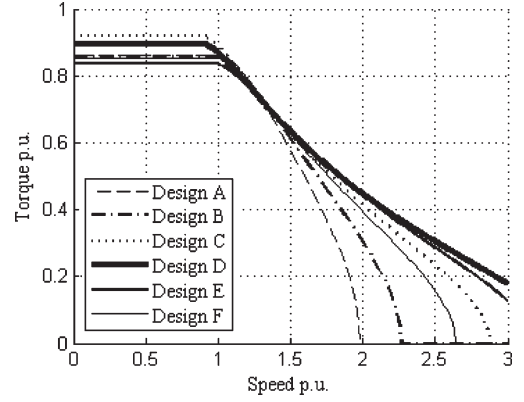

Fig. 6. Machines' static torques as a function of speed for Designs A–F with a constant flux, a current limited to unity, and in the field weakening range with a 0.95-p.u. voltage.

In (8), e_{PMN} is the rated speed induced voltage. Therefore, at low speeds ($n \leq n_{rated}$), the current angle should follow the following relation γ_{opt1}:

$$\gamma_{opt1} = \arccos \left[\frac{-e_{PMN} i_s}{4 i_s^2 \omega_s (L_{sd} - L_{sq})} \right.$$
$$\left. + \frac{\sqrt{(e_{PMN} i_s)^2 + 8 (\omega_s (L_{sq} - L_{sd}))^2 i_s^4}}{4 i_s^2 \omega_s (L_{sd} - L_{sq})} \right]. \tag{9}$$

At the rated speed, the voltage is almost equal to the maximum available voltage with some voltage reserve, for instance, $u_s = 0.95$ p.u. leaves a 5% reserve for dynamic torque changes. Above the rated speed, keeping the per-unit voltage u_s constant gives the current angle that should be followed by the motor drive controller. The optimized current angle can be determined from the following equation:

$$u_{rated}^2 = n^2 \left\lfloor (e_{PMN} + \omega_s L_{sd} i_s \cos \gamma_{opt2})^2 \right.$$
$$\left. + (\omega_s L_{sq} i_s \sin \gamma_{opt2})^2 \right\rfloor \tag{10}$$

where γ_{opt2} and X are defined in (11), shown at the bottom of the page.

In some situations, when ψ_{PM} is relatively low in per unit and smaller than the d-axis inductance L_d, the stator current can be controlled with a maximum-torque-per-voltage method [24], [25] to get more torque and power at highest speeds.

Following the preceding equations, the torques and the power capability curves for Designs A–F are plotted in Figs. 6 and 7, respectively.

$$\gamma_{opt2} = \arccos \left[\frac{-2 e_{PMN} \omega_s L_{sd} i_s}{2 i_s^2 \omega_s^2 (L_{sd}^2 - L_{sq}^2)} + \frac{X}{2 i_s^2 \omega_s^2 (L_{sd}^2 - L_{sq}^2)} \right],$$

$$X = \sqrt{(2 e_{PMN} \omega_s L_{sd} i_s)^2 - 4 i_s^2 \omega_s^2 (L_{sd}^2 - L_{sq}^2) \left(\omega_s^2 L_{sq}^2 i_s^2 + e_{PMN}^2 - \frac{u_s^2}{n^2} \right)^2} \tag{11}$$
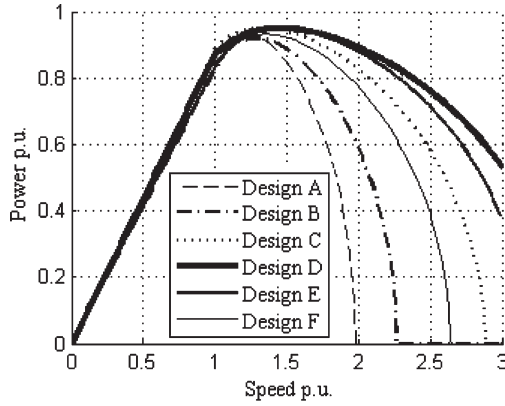
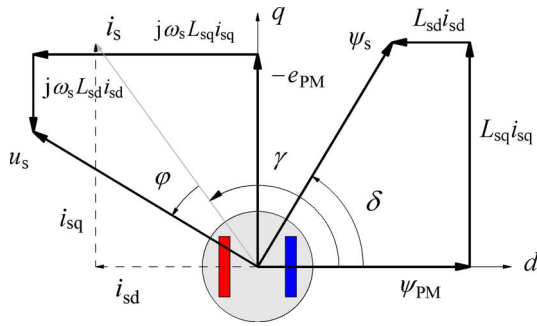Fig. 7. Power capability curves for the different machine designs as a function of speed with a rated current.

Fig. 8. Rated speed, i.e., $\omega_s = 1$ p.u. $\psi_{PM} = 0.77$ p.u., $\psi_s = 0.95$ p.u., $i_s = 1$ p.u., $u_s = 0.95$ p.u., $T_e = 0.9$ p.u., $P_e = 0.9$ p.u., $L_{sd} = 0.49$ p.u., $L_{sq} = 1$ p.u., $\gamma = 126°$, $\varphi = 23°$, and $\delta = 59°$. The stator resistance is neglected.

According to Fig. 7, the power of Design A reaches zero at a speed two times the rated speed. The powers of Designs D and E, instead, are positive, even at three times the rated speed. Correspondingly, Designs B, C, and F cannot provide a torque anymore at a 3.0-p.u. speed. We may conclude that Designs D and E can meet the boundary conditions and reach the maximum speed, which is three times the rated speed. Since Design D has slightly higher power, torque, and rotor saliency than Design E, it is chosen as the final motor design.

To achieve a high enough speed range, the difference between $|\psi_{PM}|$ and $|L_d|$ should be selected suitably small. This explains why Design D ($\psi_{PM} - L_d = 0.28$, $L_q/L_d = 2$) has a better power capability curve compared with Design E ($\psi_{PM} - L_d = 0.3$, $L_q/L_d = 1.9$).

IV. MACHINE OPERATION

Fig. 8 shows the vector diagram at a base speed ($\omega_s = 1$ p.u.). The rated current $i_s = 1$ p.u. is used, and the angle of the current vector is adjusted to obtain $\psi_s = 0.95$ p.u.. The torque output at this time instant is 0.9 p.u., and the power factor is 0.92.

The proportion of the reluctance torque in this case is calculated from (3) as

$$T_{e,\text{rel}} = (0.49 - 1) \cdot (-0.59) \cdot 0.81 = 0.24 \text{ p.u.} \quad (12)$$

To observe the behavior of the machine in the field weakening at the maximum speed ($\omega_s = 3$ p.u.), the current vector i_s is
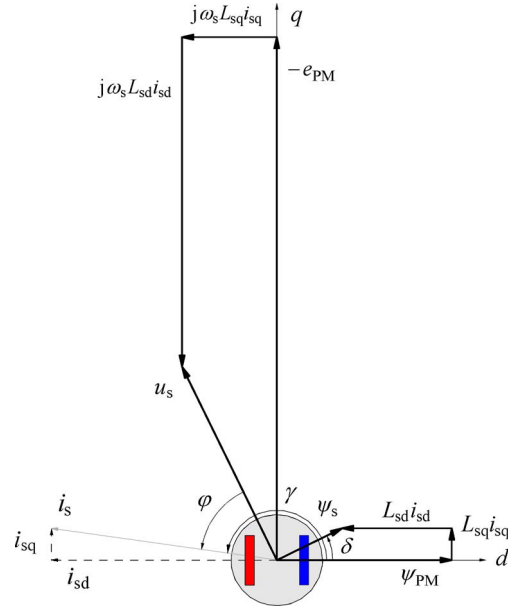

Fig. 9. High speed, i.e., $\omega_s = 3$ p.u., $\psi_{PM} = 0.77$ p.u., $\psi_s = 0.313$ p.u., $i_s = 1$ p.u., $u_s = 0.94$ p.u., $T_e = 0.18$ p.u., $P_e = 0.54$ p.u., $L_{sd} = 0.49$ p.u., $L_{sq} = 1$ p.u., $\gamma = 172°$, $\varphi = 56°$, and $\delta = 26°$. The stator resistance is neglected.
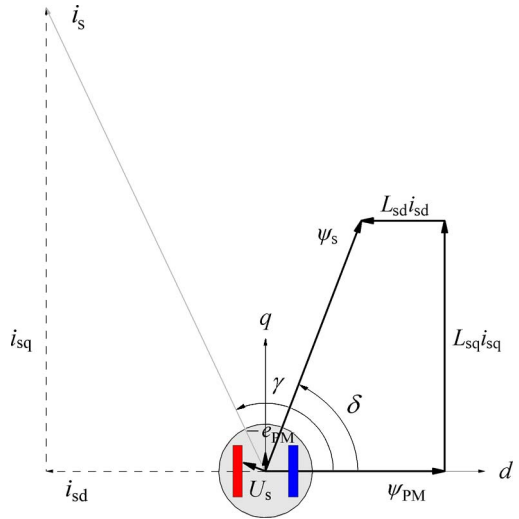

Fig. 10. Vector diagram at low speed $\omega_s = 0.1$ p.u. with high torque. $\psi_{PM} = 0.77$ p.u., $\psi_s = 1.15$ p.u., $i_s = 2.2$ p.u., $u_s = 0.15$ p.u., $T_e = 1.82$ p.u., $P_e = 0.182$ p.u., $L_{sd} = 0.38$ p.u., $L_{sq} = 0.54$ p.u., $\gamma = 115°$, $\varphi = 44°$, and $\delta = 69°$. The stator resistance is neglected.

adjusted to reduce the stator flux linkage vector ψ_s (see Fig. 9). At the maximum speed, the stator flux linkage is defined as

$$\psi_s = \psi_{PM} + L_{sd}i_{sd} = 0.77 + 0.49(-0.99) = 0.28 \text{ p.u.} \quad (13)$$

At three times the rated speed, the induced phase stator back EMF is

$$e_s = \psi_s\omega_s = 0.28 \cdot 3 = 0.84 \text{ p.u.} \quad (14)$$

The next objective is to obtain 1.8 times the rated torque to crank the ICE for starting. This can be achieved by increasing the magnitude of the stator current and the air gap flux linkage to fully utilize the reluctance torque. The inductance values

TABLE III
MACHINE DESIGN DATA

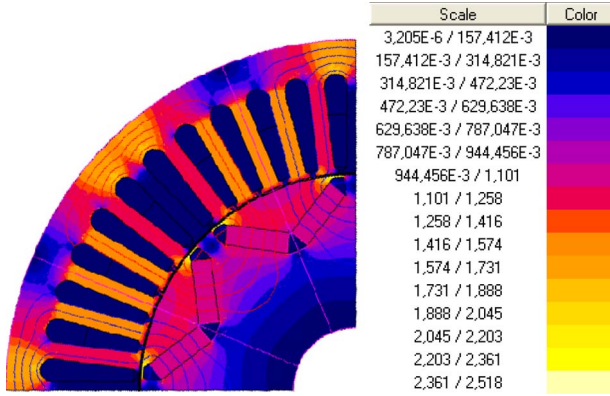| Parameter	Value	Unit
Stator outer diameter, D_{se}	252	mm
Stator inner diameter, D_s	156.4	mm
Rotor outer diameter, D_r	155	mm
Rotor inner diameter, D_{ri}	80	mm
Stator stack length, l	40	mm
Number of winding turns, N_s	56	-
Number of stator slots, Q_s	48	-
Winding pitch, W/τ_p	5/6	-
PM height, h_{PM}	9	mm
PM width, w_{PM}	23	mm

Fig. 11. Flux lines and flux density plot in different parts of the machine.

will change at this point because of saturation. Fig. 10 shows the vector diagram with inductances numerically calculated when the stator current is equal to 2 p.u. The magnitude of the stator current was increased until the torque was 1.8 times the rated value. According to the vector diagram, the stator current should be at least 2.2 p.u. at the cranking speed ($\omega_s = 0.1$ p.u.).

V. FEA DESIGN

The main dimensions of the final motor design are given in Table III.

A. No-Load Operation

In no-load operation, the machine rotates at the nominal speed, i.e., 1500 min^{-1}. Fig. 11 illustrates the no-load flux lines and the flux density plot in different regions of the machine. The open-circuit flux densities remain relatively small as the PM flux is only 77% of the stator rated flux.

The air gap flux density distribution is presented in Fig. 12. The fundamental peak value of the induced phase voltage is 53.3 V; and the corresponding RMS value is 37.7 V, which is 77% of the rated voltage.
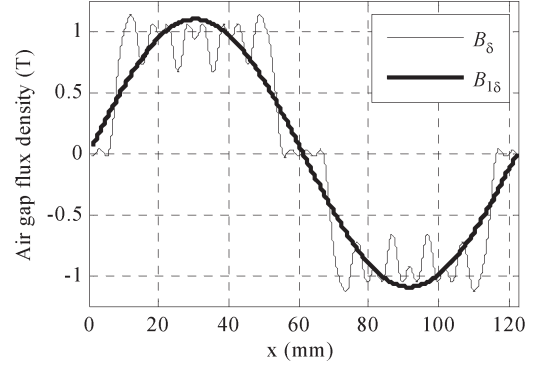

Fig. 12. Distribution of the air gap flux density. The fundamental peak value of the air gap flux density is 1.095 T.

B. Load

The on-load operation analysis is carried out to calculate the motor efficiency at nominal power.

The mechanical losses or a sum of windage and ventilator losses are estimated according to [26] as

$$P_{\text{mech}} = k_\rho D_r (l_r + 0.6\tau_p)\nu_r \qquad (15)$$

where k_ρ is an experimental factor (for an open-circuit cooling, as in this case, small- and medium-sized machines $k_\rho = 10$ Ws^2/m^4); D_r is the outer rotor diameter; l_r is the rotor length; τ_p is the pole pitch; and v_r is the surface speed of the rotor, which can be given by $v_r = \pi n D_r$.

The stator losses are the Joule losses and are expressed as

$$P_{s,\text{Cu}} = m I_s^2 R_s \qquad (16)$$

where m is the number of phases, I_s is the stator phase current, and R_s is the stator phase resistance.

The stator iron losses are calculated by an FEA. Flux 2D estimates the stator laminated iron losses P_{Fe} by

$$
\begin{aligned}
P_{\text{Fe}} &= \frac{1}{T}\int_0^T P_{\text{Fe}}(t)\,dt \\
&= k_h \hat{B}^2 f k_f \\
&\quad + \frac{1}{T}\int_0^T k_f \left[\sigma_{\text{Fe}} \frac{d^2}{12}\left(\frac{dB(t)}{dt}\right)^2 + k_e \left(\frac{dB(t)}{dt}\right)^{1.5} \right] dt
\end{aligned}
$$

$$(17)$$

where $\hat{B}$ is the maximum flux density in the element concerned, B is the instantaneous flux density, f is the frequency, σ_{Fe} is the conductivity, d is the lamination sheet thickness, k_h is the hysteresis loss coefficient, k_e is the excess loss coefficient, and k_f is the iron space factor.

In the calculation, the additional losses are assumed to be 1% of the output mechanical power. Table IV gives the computation results of losses and efficiency at the rated speed of 1500 min^{-1} and at a high speed of 4500 min^{-1}. The torques at the corresponding speeds are 58 and 18.3 Nm.

TABLE IV
MACHINE DESIGN DATA AT 10 KW

Speed	1500 min⁻¹	4500 min⁻¹
Stator copper losses, $P_{s,Cu}$	735 W	735 W
Stator iron losses, $P_{s,Fe}$	52 W	312 W
Mechanical losses, P_{mech}	24 W	219 W
Additional losses, P_{add}	100 W	100 W
Total losses, P_{loss}	911 W	1366 W
Efficiency, η	91.7 %	88 %

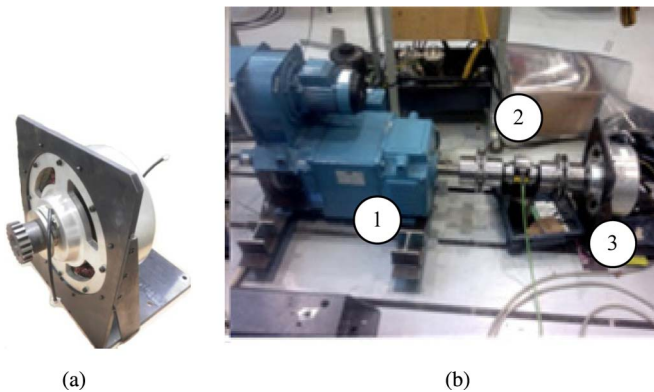Fig. 13. Rotor and stator laminations.

(a)　　　　　　　　(b)

Fig. 14. (a) Assembled motor and (b) laboratory test setup for the experimental test. (1) DC machine acting as a prime mover in the no-load and generator tests and the machine load in the load test. (2) Torque transducer. (3) Prototype of the designed PMSM.

VI. EXPERIMENTAL RESULTS

Based on the electromagnetic design, a prototype for the experimental tests was manufactured. The rotor and stator laminations are illustrated in Fig. 13. The lamination material used in the stator and the rotor was a 0.5-mm-thick steel sheet of M350-50A. The PMs in the rotor have remanent a flux density of 1.08 T and coercive force of 826 kA/m. The assembled motor is shown in Fig. 14(a). The laboratory test setup is illustrated in Fig. 14(b).

The machine was driven by a 400-V industrial frequency converter with active network bridge to also enable generator operation. The dc bus voltage of 600 V was used instead of 120 V, which is the car energy storage design voltage. Sufficient filtering and current smoothing were ensured to protect the machine from high-voltage stresses. The terminal voltage of the machine was maintained at its rated level. A four-quadrant dc
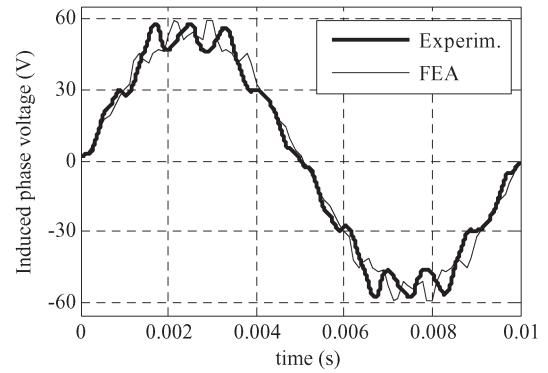

Fig. 15. No-load voltage at the rated speed as a function of time.

TABLE V
PERFORMANCE RESULTS AT RATED SPEED IN MOTOR OPERATION

n, min⁻¹	U, V	I, A	T, Nm	$\cos\varphi$	η
1498	39.8	23.2	15.2	0.99	0.82
1496	42.4	45.5	31.3	0.94	0.87
1496	45.8	69.8	47.1	0.88	0.86
1496	49.7	86.1	53.8	0.70	0.8
1500	48.8	101.5	64.8	0.79	0.86

TABLE VI
PERFORMANCE RESULTS AT RATED SPEED IN GENERATOR OPERATION

n, min⁻¹	U, V	I, A	T, Nm	$\cos\varphi$	η
1495	38.4	22.9	17.5	0.97	0.82
1496	39.2	45.4	34.2	0.91	0.87
1495	43.8	71.2	51.2	0.77	0.85
1442	40.2	97	67.5	0.78	0.90

drive was connected to the shaft of the PMSM, and it acted as a load or mechanical power source to the machine.

The following tests were carried out to evaluate the performance of the machine at different operating points.

A. No-Load Test

The no-load terminal voltage was measured at the rated speed of 1500 min⁻¹ (see Fig. 15). The no-load phase voltage fundamental RMS value E_{PM} is 38.3 V, which corresponds to 0.78 p.u. The high harmonic content of the machine is a result of a non-skewed magnetic circuit.

B. Load Test

The machine is operated at the rated speed both as a motor and a generator. The measurement values are given in Tables V–VIII (see Appendix). Since the drive was operated by using a 600-V dc bus voltage, there is a considerable amount of voltage ripple in the supply (see Fig. 16). Fig. 17 compares the experimental and calculated results of the torque versus current both at low and rated speeds.

TABLE VII
PERFORMANCE RESULTS AT LOW SPEED IN MOTOR OPERATION

n, min^{-1}	U, V	I, A	T, Nm	$\cos \varphi$	η
746.9	19.9	22.8	15.5	0.99	0.82
746.7	20.6	46.7	31.7	0.97	0.86
747.0	23.3	67.0	46.9	0.91	0.83

TABLE VIII
PERFORMANCE RESULTS AT LOW SPEED IN GENERATOR OPERATION

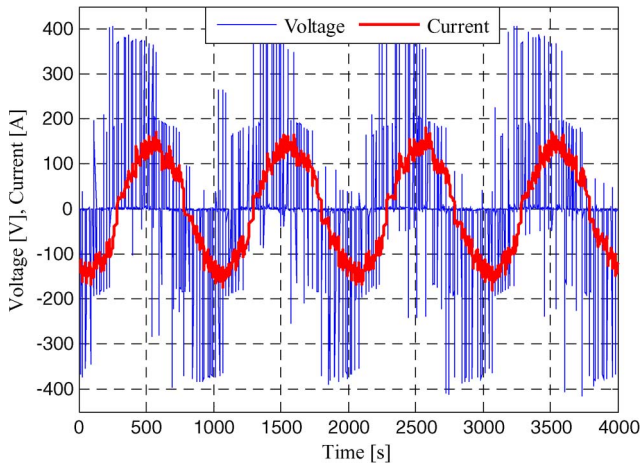| n, min^{-1}	U, V	I, A	T, Nm	$\cos \varphi$	η
747.0	23.3	22.2	17.2	0.97	0.81
746.6	20.1	44.3	33.8	0.90	0.85
746.6	20.9	69.5	50.7	0.73	0.80

Fig. 16. Test motor pulsewidth-modulated supply voltage and one phase current. The motor is running 1500 min^{-1} with a rated torque. The voltage spikes are high because of the 600-V dc-link voltage.
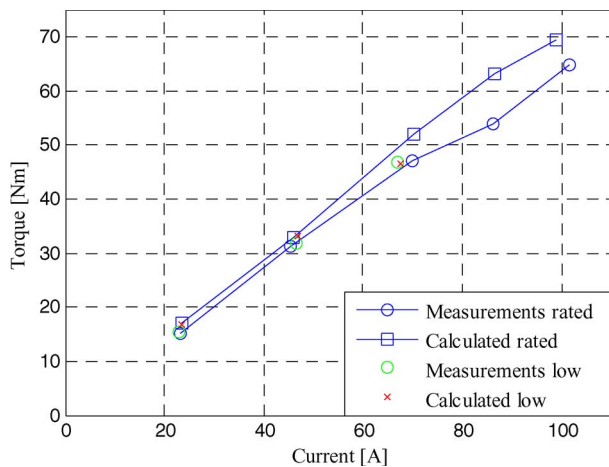

Fig. 17. Torque versus current at low and rated speeds.

In Fig. 17, it is observed that the calculated curve of the torque as a function of the current is linear and has a constant slope up to the rated current, beyond which its slope decreases. This is due to the saturation of the machine at high current. The torque per ampere slightly decreases beyond this point. This phenomenon is also evident in the measurements.
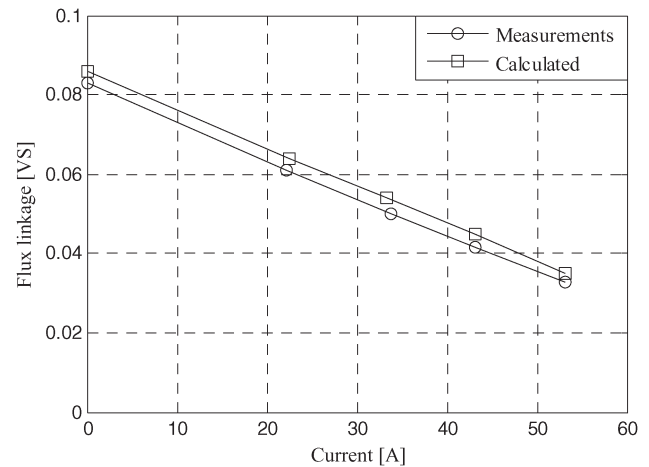

Fig. 18. Calculated and measured d-axis flux linkage versus stator current at a 1500-min^{-1} speed.
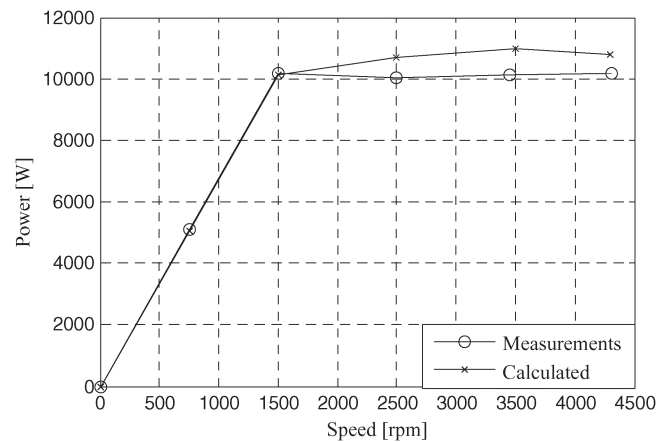

Fig. 19. Calculated and measured power as the function of speed.

C. Field Weakening Test

The machine was operated in the constant-power region. In order to find the field weakening range of the machine, it was tested at the rated speed. The machine was run at 1500 min^{-1}, and different values of flux reference were manually fed to the drive.

Fig. 18. demonstrates the flux-weakening capability of the machine. It shows the experimental and calculated values of d-axis flux linkage as a function of the stator current at a 1500-min^{-1} speed. When the stator current is equal to zero (no-load condition), the value of the flux linkage corresponds to ψ_{PM}. As the magnitude of the current increases, the flux linkage of the machine decreases, and it is evident that the flux linkage of the machine can be reduced to one third, proving the feasibility to operate at high speed. The magnitude of the current I_d is still less than the rated current; this implies that the machine can produce some torque, even at this flux level, by injecting I_q.

Power, torque, and efficiency as the function of rotational speed are presented in Figs. 19–21, respectively.

It is observed that the calculation and measurement results increasingly differ from each other as the flux linkage of the machine increases (see Fig. 20). This is also evident in
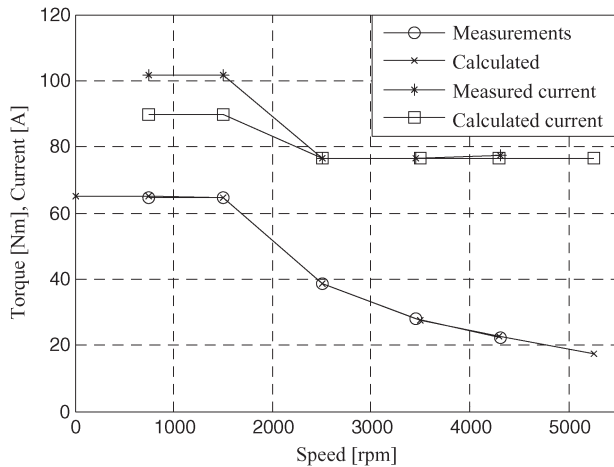
Fig. 20.   Calculated and measured torque and stator current versus rotational speed.
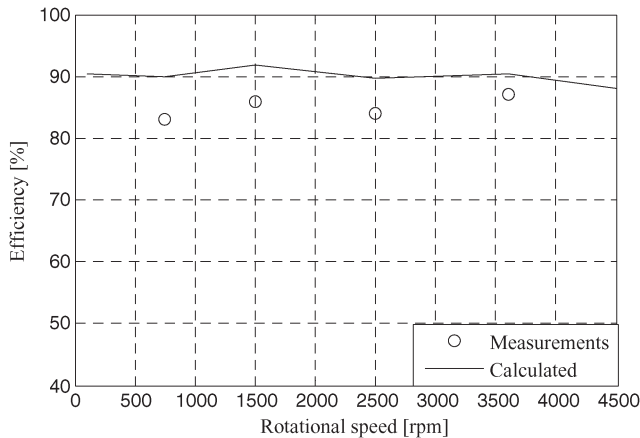

Fig. 21.   Calculated and measured efficiency as the function of speed.

Fig. 17, where a similar difference can be observed. For the same value of torque, the experimental measurement indicates a higher current value than the calculated value. The reason for the difference is obviously that the machine saturates and the calculated flux linkage is therefore higher than the actual value. The temperature during the calculation might be also one reason that could have an effect to the flux linkage and thus to the low value of the calculated current.

The 10-kW prototype gave the performance as expected, given the design requirement. The high-voltage harmonic content resulted in slightly lower efficiency than expected.

The design guidelines proposed in this research for a wide speed range of operation helped to achieve the performance for different speeds. A machine was designed and built following this procedure and was tested at different speeds with a reasonable good agreement between predicted and experimental results. The flux weakening range of the machine was also demonstrated to indicate its maximum high-speed capability. Thus, this design approach can be used to design similar kinds of drives for hybrid or traction applications.

VII. CONCLUSION

This paper have studied the design principles of PMSMs for parallel hybrid or traction applications. Necessary boundary

conditions, such as permanent magnet flux linkage level and the synchronous inductances, were discussed. Several different topologies capable of producing a low-speed peak torque of 1.8 p.u. and a maximum speed of 3 p.u. were studied. Suitable inductances for machine operation were considered. A practical flux barrier design to maximize the inductance difference was chosen for further study and prototyping.

Next, by means of numerical solution, which is based on an FEA, the dynamic behavior of the designed motor was investigated. Three different operation points (no load, rated operation, and short circuit) were analyzed.

Finally, based on the results from the numerical solution, an experimental prototype of the PMSM was built. The prototype was tested both in generator and motor modes. The experimental results verified the operation of the designed PMSM for parallel hybrid or traction applications. Thus, the basic design principles were validated.

APPENDIX

Measurement values of the machine operated at the rated speed and at low speed both as a motor and a generator are presented here. Tables V–VIII.

ACKNOWLEDGMENT

REFERENCES

[1] S. S. Williamson, S. M. Lukic, and A. Emadi, "Comprehensive drive train analysis of hybrid electric and fuel cell vehicles based on motor-controller efficiency modeling," *IEEE Trans. Veh. Technol.*, vol. 21, no. 3, pp. 730–740, May 2006.

[2] P. H. Nguyen, E. Hoang, and M. Gabsi, "Performance synthesis of permanent-magnet synchronous machines during the driving cycle of a hybrid electric vehicle," *IEEE Trans. Veh. Technol.*, vol. 60, no. 5, pp. 1991–1998, Jun. 2011.

[3] P. Immonen, L. Laurila, and J. Pyrhönen, "Modelling of a diesel–electric parallel hybrid drive system in MATLAB Simulink," *Int. Rev. Model. Simul.(IREMOS)*, vol. 2, no. 5, p. 565, Oct. 2009.

[4] Cited on the 19th of March 2012 http://www.inrets.fr

[5] A. Emadi, K. Rajashekara, S. S. Williamson, and S. M. Lukic, "Topological overview of hybrid electric and fuel cell vehicular power system architectures and configurations," *IEEE Trans. Veh. Technol.*, vol. 54, no. 3, pp. 763–770, May 2005.

[6] C. C. Chan, "The state of the art of electric, hybrid, and fuel cell vehicles," *Proc. IEEE*, vol. 97, no. 4, pp. 704–718, Apr. 2007.

[7] C. C. Chan, A. Bouscayrol, and K. Chen, "Electric, hybrid, and fuel-cell vehicles: Architectures and modeling," *IEEE Trans. Veh. Technol.*, vol. 59, no. 2, pp. 589–598, Feb. 2010.

[8] W. L. Soong, S. Han, and T. M. Jahns, "Design of interior PM machines for field-weakening applications," in *Conf. Rec. ICEM*, Seoul, Korea, Oct. 8–11, 2007, pp. 654–664.

[9] T. L. Seong, "Development and analysis of interior permanent magnet synchronous motor with field excitation structure," Ph.D. dissertation, Univ. Tennessee, Knoxville, TN, 2009.

[10] C. Liu, K. T. Chau, and J. Z. Jiang, "A permanent-magnet hybrid brushless integrated starter-generator for hybrid electric vehicles," *IEEE Trans. Ind. Electron.*, vol. 57, no. 12, pp. 4055–4064, Dec. 2010.

[11] K. I. Laskaris and A. G. Kladas, "Internal permanent magnet motor design for electric vehicle drive," *IEEE Trans. Ind. Electron.*, vol. 57, no. 1, pp. 138–145, Jan. 2010.

[12] Y. K. Chin and J. Soulard, "A permanent magnet synchronous motor for traction applications of electric vehicles," in *Proc. IEEE IEMDC*, 2003, pp. 1035–1041.

[13] J. J. Germishuizen and M. J. Kamper, "IPM traction machine with single layer non-overlapping concentrated windings," *IEEE Trans. Ind. Appl.*, vol. 45, no. 4, pp. 1387–1394, Jul./Aug. 2009.

[14] J.-H. Cho, H.-S. Oh, S.-U. Cho, D. G. Kim, and I.-S. Park, "Development of IPM synchronous motor for diesel hybrid electric vehicle," in *Proc. INTELEC*, 2009, pp. 1–5.

[15] M. Barcaro, N. Bianchi, and F. Magnussen, "Permanent-magnet optimization in permanent-magnet-assisted synchronous reluctance motor for a wide constant-power speed range," *IEEE Trans. Ind. Electron.*, vol. 59, no. 6, pp. 2495–2502, Jun. 2012.

[16] S. Chaithongsuk, B. Nahid-Mobarakeh, J.-P- Caron, N. Takorabet, and F. Meiroby-Tabar, "Optimal design of permanent magnet motors to improve field-weakening performances in variable speed drives," *IEEE Trans. Ind. Electron.*, vol. 59, no. 6, pp. 2484–2494, Jun. 2012.

[17] D. G. Dorrell, A. M. Knight, L. Evans, and M. Popescu, "Analysis and design techniques applied to hybrid vehicle drive machines—Assessment of alternative IPM and induction motor topologies," *IEEE Trans. Ind. Electron.*, vol. 59, no. 10, pp. 3690–3699, Oct. 2012.

[18] T. Finken, M. Hombitzer, and K. Hameyer, "Study and comparison of several permanent-magnet excited rotor types regarding their applicability in electric vehicles," in *Proc. Emobility—Elect. Power Train*, 2010, pp. 1–7.

[19] W. Aimeng, J. Yihua, and W. L. Soong, "Comparison of five topologies for an interior permanent-magnet machine for a hybrid electric vehicle," *IEEE Trans. Magn.*, vol. 47, no. 10, pp. 3606–3609, Oct. 2011.

[20] M. E. Hall and J. C. Balda, "Permanent magnet synchronous motor drive for HEV propulsion: Optimum speed ratio and parameter determination," in *Proc. IEEE 56th VTC*, 2002, pp. 1500–1504.

[21] K. Khan, S. Haghbin, M. Leksell, and O. Wallmark, "Design and performance analysis of a permanent-magnet assisted synchronous reluctance machine for an integrated charger application," in *Proc. ICEM*, Rome, Italy, 2010, pp. 1–6.

[22] J. Pyrhönen, T. Jokinen, and T. V. Hrabovcová, *Design of Rotating Electrical Machine*. Chichester, U.K.: Wiley, 2008.

[23] R. Schiferl and T. A. Lipo, "Power capability of salient pole permanent magnet synchronous motors in variable speed drive applications," *IEEE Trans. Ind. Appl.*, vol. 26, no. 1, pp. 115–123, Jan./Feb. 1990.

[24] B. Cheng and T. R. Tesch, "Torque feedforward control technique for permanent-magnet synchronous motors," *IEEE Trans. Ind. Electron.*, vol. 57, no. 3, pp. 969–974, Mar. 2010.

[25] H. Lei, Z. Gumming, and H. Peng, "An approach to improve the torque performance of IPMSM by considering cross saturation applied for hybrid electric vehicle," in *Proc. ICEMS*, Incheon, Korea, Oct. 10–13, 2010, pp. 1378–1381.

[26] W. Schuisky, *Design of Electrical Machines (Berechnung Elektrischer Maschinen)*. Vienna, Austria: Springer-Verlag, 1960.

Mahendarkar Prabhakaran Ragavendra received the B.E degree in electrical and electronics engineering from the University of Madras, Chennai, India, in 2004, and the M.Sc. degree in electrical engineering from Lappeenranta University of Technology, Lappeenranta, Finland, in 2012.

He is currently working as a Senior Development Engineer with Lucas-TVS Ltd., Chennai, which is an auto electrical company. His research interests are in the fields of electrical machines, design of permanent magnet synchronous machines, claw-pole synchronous machines, and electromagnetic analysis.

Juha Pyrhönen (M'06) received the D.Sc. degree from Lappeenranta University of Technology (LUT), Lappeenranta, Finland, in 1991.

In 1993 and 1997, he became an Associate Professor of electrical engineering and a Professor of electrical machines and drives, respectively, with LUT, where he is currently the Head of the Department of Electrical Engineering and engaged in the research and development of electric motors and electric drives. His current research interests include different synchronous machines and drives, induction motors and drives, and solid-rotor high-speed induction machines and drives.

Juan A. Tapia (M'03) received the B.Sc. and M.Sc. degrees in electrical engineering from the University of Concepcion, Concepcion, Chile, in 1991 and 1997, respectively, and the Ph.D. degree from the University of Wisconsin, Madison, in 2002.

Since 1992, he has started to work with the Department of Electrical Engineering, University of Concepcion, where he is currently an Associate Professor. Since 2010, he has been a Finland Distinguished Professor Fellow from the Academy of Finland with Lappeenranta University of Technology (LUT), where he conducts research on permanent magnet machine on LUT-Energia Group. His primary research areas are electrical machine design, numerical method for electromagnetic field, digital-signal-processor-based electric machine control, and renewable energy.

Katteden Kamiev received the B.Sc. and M.Sc. degrees in electrical engineering from St. Petersburg State Polytechnic University, Saint-Petersburg, Russia, in 2006 and 2008, respectively, and the M.Sc. degree in electrical engineering (double degree program) in 2008 from Lappeenranta University of Technology, Lappeenranta, Finland, where he is currently working toward the Ph.D. degree.

His research interests are traditional synchronous machines, permanent magnet synchronous machines, and hybrid excitation synchronous machines and their damping features.

Juho Montonen received the B.Sc. and M.Sc. degrees in electrical engineering in 2011 and 2012, respectively, from Lappeenranta University of Technology, Lappeenranta, Finland, where he is currently working toward the Ph.D. degree, doing research about electrical machines and drives.

His research work focuses on permanent magnet synchronous motors, particularly the ones used in different kinds of traction applications.

Markku Niemelä received the B.Sc. degree in electrical engineering from Helsinki Institute of Technology, Helsinki, Finland, in 1990 and the M.Sc. and D.Sc. degrees from Lappeenranta University of Technology (LUT), Lappeenranta, Finland, in 1995 and 1999, respectively.

He is currently a Senior Researcher with the Carelian Drives and Motor Centre in LUT. His current research interests include motion control, control of line converters, and energy efficiency of electric drives.